

# The role of viscosity on drop impact forces

Vatsal Sanjay<sup>1†</sup>, Bin Zhang<sup>2‡</sup>, Cunjing Lv<sup>2¶</sup>, and Detlef Lohse<sup>1,3||</sup>

<sup>1</sup>Physics of Fluids Group, Max Planck Center for Complex Fluid Dynamics, Department of Science and Technology, and J. M. Burgers Centre for Fluid Dynamics, University of Twente, P. O. Box 217, 7500 AE Enschede, The Netherlands

<sup>2</sup>Department of Engineering Mechanics, AML, Tsinghua University, Beijing 100084, China

<sup>3</sup>Max Planck Institute for Dynamics and Self-Organization, Am Fassberg 17, 37077 Göttingen, Germany

(Received xx; revised xx; accepted xx)

A liquid drop impacting a rigid substrate undergoes deformation and spreading due to normal reaction forces, which are counteracted by surface tension. On a non-wetting substrate, the drop subsequently retracts and takes off. Our recent work (Zhang et al., *Phys. Rev. Lett.*, vol. 129, 2022, 104501) revealed two peaks in the temporal evolution of the normal force  $F(t)$ —one at impact and another at jump-off. The second peak coincides with a Worthington jet formation, which vanishes at high viscosities due to increased viscous dissipation affecting flow focusing. In this article, using experiments, direct numerical simulations, and scaling arguments, we characterize both the peak amplitude  $F_1$  at impact and the one at take off ( $F_2$ ) and elucidate their dependency on the control parameters: the Weber number  $We$  (dimensionless impact velocity) and the Ohnesorge number  $Oh$  (dimensionless viscosity). The first peak amplitude  $F_1$  and the time  $t_1$  to reach it depend on inertial timescales for low viscosity liquids, remaining nearly constant for viscosities up to 100 times that of water. For high viscosity liquids, we balance the rate of change in kinetic energy with viscous dissipation to obtain new scaling laws:  $F_1/F_\rho \sim \sqrt{Oh}$  and  $t_1/\tau_\rho \sim 1/\sqrt{Oh}$ , where  $F_\rho$  and  $\tau_\rho$  are the inertial force and time scales, respectively, which are consistent with our data. The time  $t_2$  at which the amplitude  $F_2$  appears is set by the inertia-capillary timescale  $\tau_\gamma$ , independent of both the viscosity and the impact velocity of the drop. However, these properties dictate the magnitude of this amplitude.

**Key words:**

---

## 1. Introduction

Drop impacts have piqued the interest of scientists and artists alike for centuries, with the phenomenon being sketched by da Vinci (1508) in the early 16<sup>th</sup> and photographed by Worthington (1876a,b) in the late 19<sup>th</sup> century. It is, indeed, captivating to observe raindrops hitting a solid surface (Kim et al. 2020; Lohse & Villermaux 2020) or ocean spray affecting maritime structures (Berny et al. 2021; Villermaux et al. 2022). The phenomenology of drop impact is extremely rich, encompassing behaviors such as drop

† Email address for correspondence: vatsalsanjay@gmail.com

‡ Email address for correspondence: binzhang0710@mail.tsinghua.edu.cn

¶ Email address for correspondence: cunjinglv@mail.tsinghua.edu.cn

|| Email address for correspondence: d.lohse@utwente.nl

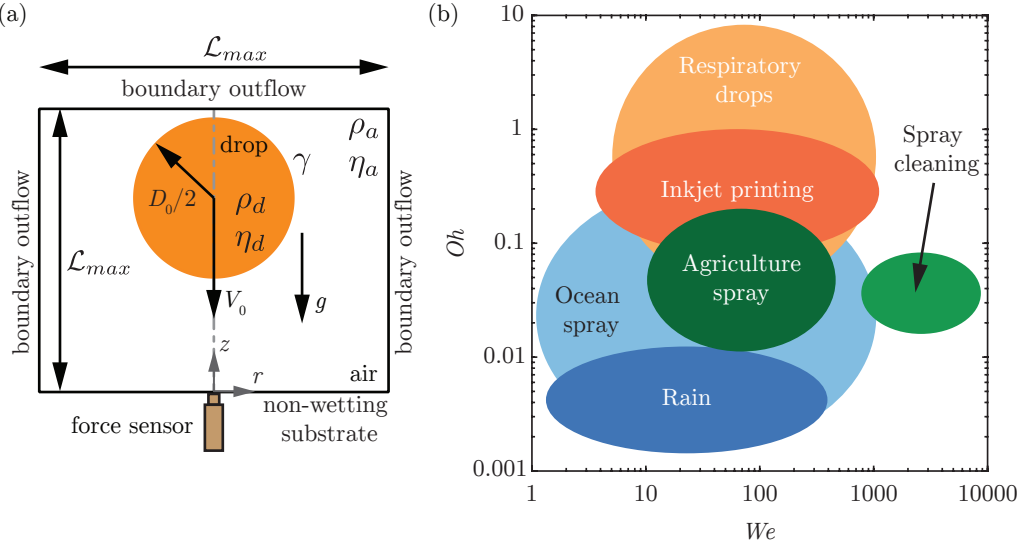


FIGURE 1. (a) Problem schematic with an axisymmetric computational domain used to study the impact of a drop with diameter  $D_0$  and velocity  $V_0$  on a non-wetting substrate. In the experiments, we use a quartz force sensor to measure the temporal variation of the impact force. The subscripts  $d$  and  $a$  denote the drop and air, respectively, to distinguish their material properties, which are the density  $\rho$  and the dynamic viscosity  $\eta$ . The drop-air surface tension coefficient is  $\gamma$ . The grey dashed-dotted line represents the axis of symmetry,  $r = 0$ . Boundary air outflow is applied at the top and side boundaries (tangential stresses, normal velocity gradient, and ambient pressure are set to zero). The domain boundaries are far enough from the drop not to influence its impact process ( $L_{\max} \gg D_0$ ,  $L_{\max} = 8R$  in the worst case). (b) The phase space with control parameters: the Weber number ( $We$ : dimensionless impact velocity) and the Ohnesorge number ( $Oh$ : dimensionless viscosity), exemplifying different applications.

deformation (Biance *et al.* 2006; Moláček & Bush 2012; Chevy *et al.* 2012), spreading (Laan *et al.* 2014; Wildeman *et al.* 2016), splashing Xu *et al.* (2005); Riboux & Gordillo (2014); Thoraval *et al.* (2021), fragmentation (Villermaux & Bossa 2011; Villermaux 2020), bouncing (Richard & Quéré 2000; Kolinski *et al.* 2014; Jha *et al.* 2020; Chubytsky *et al.* 2020; Sharma & Dixit 2021; Sanjay *et al.* 2023a), and wetting (de Gennes 1985; Fukai *et al.* 1995; Quéré 2008; Bonn *et al.* 2009). These behaviors are influenced by the interplay of inertial, capillary, and viscous forces, as well as additional factors like non-Newtonian properties (Bartolo *et al.* 2005, 2007; Smith & Bertola 2010; Gorin *et al.* 2022) of the liquid and even ambient air pressure (Xu *et al.* 2005), making the parameter space for this phenomenon both extensive and high-dimensional.

Naturally, even the process of a Newtonian liquid drop impacting a rigid substrate is governed by a plethora of control parameters, including but not limited to the drop's density  $\rho_d$ , diameter  $D_0$ , velocity  $V_0$ , dynamic viscosity  $\eta_d$ , surface tension  $\gamma$ , and acceleration due to gravity  $g$  (figure 1a). To navigate this rich landscape, we focus on two main dimensionless numbers that serve as control parameters (figure 1b): the Weber number  $We$ , which is the ratio of inertial to capillary forces and is given by

$$We = \frac{\rho_d V_0^2 D_0}{\gamma}, \quad (1.1)$$

and the Ohnesorge number  $Oh$ , which captures the interplay between viscous damping

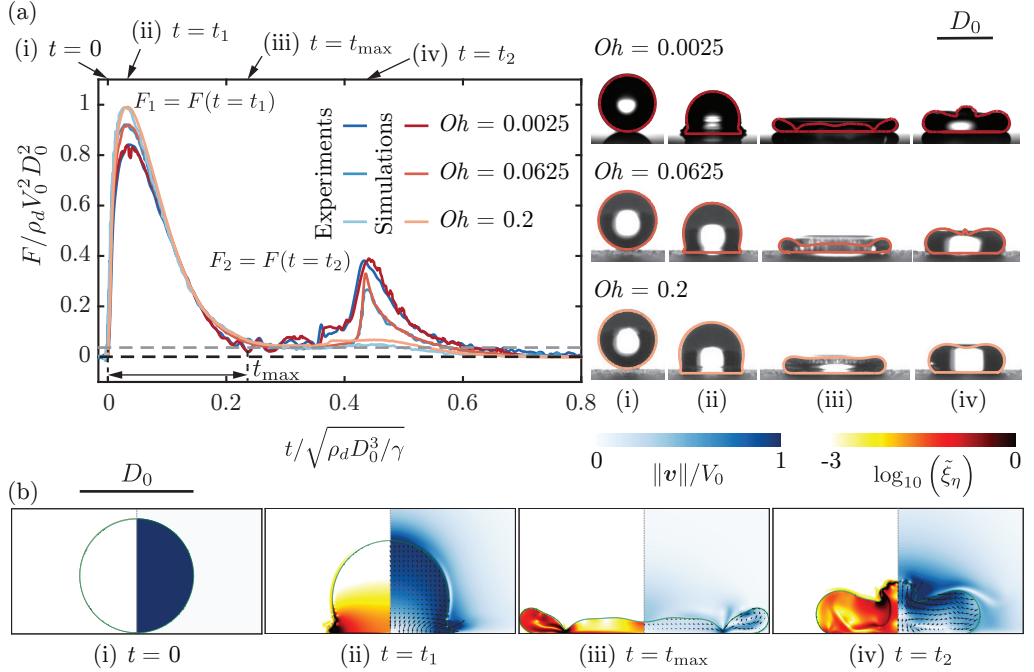


FIGURE 2. Comparison of the drop impact force  $F(t)$  obtained from experiments and simulations for the three typical cases with impact velocity  $V_0 = 1.2 \text{ m/s}, 0.97 \text{ m/s}, 0.96 \text{ m/s}$ , diameter  $D_0 = 2.05 \text{ mm}, 2.52 \text{ mm}, 2.54 \text{ mm}$ , surface tension  $\gamma = 72 \text{ mN/m}, 61 \text{ mN/m}, 61 \text{ mN/m}$  and viscosity  $\eta_d = 1 \text{ mPa s}, 25.3 \text{ mPa s}, 80.2 \text{ mPa s}$ . These parameter give  $Oh = 0.0025, 0.0625, 0.2$  and  $We = 40$ . For the three cases, the two peak amplitudes,  $F_1/\rho_d V_0^2 D_0^2 \approx 0.82, 0.92, 0.99$  at  $t_1 \approx 0.03\sqrt{\rho_d D_0^3/\gamma}$  and  $F_2/\rho_d V_0^2 D_0^2 \approx 0.37, 0.337, 0.1$  at  $t_2 \approx 0.42\sqrt{\rho_d D_0^3/\gamma}$ , characterize the inertial shock from impact and the Worthington jet before takeoff, respectively. The drop reaches the maximum spreading at  $t_{\max}$  when it momentarily stops and retracts until  $0.8\sqrt{\rho_d D_0^3/\gamma}$  when the drop takes off ( $F = 0$ ). The black and gray dashed lines in panel (a) mark  $F = 0$  and the resolution  $F = 0.5 \text{ mN}$  of our piezoelectric force transducer, respectively. (b) Four instances are further elaborated through numerical simulations for ( $We = 40, Oh = 0.0025$ ), namely (i)  $t = 0 \text{ ms}$  (touch-down), (ii)  $t = 0.37 \text{ ms}$  ( $t_1$ ), (iii)  $t = 2.5 \text{ ms}$  ( $t_{\max}$ ), and (iv)  $t = 4.63 \text{ ms}$  ( $t_2$ ). The insets of panel (a) exemplify these four instances for the three representative cases illustrated here. The experimental snapshots are overlaid with the drop boundaries from simulations. We stress the excellent agreement between experiments and simulations without any free parameters. The left part of each numerical snapshot shows the dimensionless local viscous dissipation function  $\tilde{\xi}_\eta \equiv \xi_\eta D_0 / (\rho_d V_0^3) = 2Oh (\tilde{\mathcal{D}} : \tilde{\mathcal{D}})$ , where,  $\mathcal{D}$  is the symmetric part of the velocity gradient tensor, on a  $\log_{10}$  scale and the right part the velocity field magnitude normalized with the impact velocity. The black velocity vectors are plotted in the center of mass reference frame of the drop to clearly elucidate the internal flow. Also see supplementary videos SM1-SM3.

and capillary oscillations, offering insights into how viscosity affects the drop's behavior upon impact,

$$Oh = \frac{\eta_d}{\sqrt{\rho_d \gamma D_0}}. \quad (1.2)$$

Additionally, the Bond number

$$Bo = \frac{\rho_d g D_0^2}{\gamma} \quad (1.3)$$

57 compares gravity to inertial forces and is needed to uniquely define the non-dimensional  
 58 problem.

59 The drop impact is not only interesting from the point of view of fundamental research  
 60 but also finds relevance in inkjet printing (Lohse 2022), the spread of respiratory drops  
 61 carrying airborne microbes (Bourouiba 2021; Ji *et al.* 2021; Pöhlker *et al.* 2023), cooling  
 62 applications (Kim 2007; Shiri & Bird 2017; Jowkar & Morad 2019), agriculture (Bergeron  
 63 *et al.* 2000; Bartolo *et al.* 2007; Kooij *et al.* 2018; Sijs & Bonn 2020; He *et al.* 2021;  
 64 Hoffman *et al.* 2021), criminal forensics (Smith *et al.* 2018; Smith & Brutin 2018), and  
 65 many other industrial and natural processes (Rein 1993; Yarin 2006; Tuteja *et al.* 2007;  
 66 Cho *et al.* 2016; Josserand & Thoroddsen 2016; Yarin *et al.* 2017; Liu *et al.* 2017; Hao  
 67 *et al.* 2016; Yarin *et al.* 2017; Wu *et al.* 2020). For these applications, it is pertinent to  
 68 understand the forces involved in drop impacts, as these forces can lead to soil erosion  
 69 (Nearing *et al.* 1986) or damage to engineered surfaces (Ahmad *et al.* 2013; Amirzadeh  
 70 *et al.* 2017; Gohardani 2011). We refer the readers to Cheng *et al.* (2022) for an overview  
 71 of the recent studies unraveling drop impact forces; see also Li *et al.* (2014); Soto *et al.*  
 72 (2014); Philippi *et al.* (2016); Zhang *et al.* (2017); Gordillo *et al.* (2018); Mitchell *et al.*  
 73 (2019); Zhang *et al.* (2019).

74 These forces have been studied by Zhang *et al.* (2022), employing experiments and  
 75 simulations and deriving scaling laws. A liquid drop impacting a non-wetting substrate  
 76 (figure 2i-vi) undergoes a series of phases—spreading, recoiling, and potentially rebounding  
 77 (Chantelot 2018)—driven by the normal reaction force exerted by the substrate. The  
 78 moment of touch-down (figure 2i-ii) (Wagner 1932; Philippi *et al.* 2016; Gordillo *et al.*  
 79 2018) is not surprisingly associated with a pronounced peak in the temporal evolution of  
 80 the drop impact force  $F(t)$  owing to the sudden deacceleration as high as 100 times the  
 81 acceleration due to gravity (Clanet *et al.* 2004) (figure 2,  $F(t = 0.37\text{ ms}) \approx 5.1\text{ mN}$ ). The  
 82 force diminishes as the drop reaches its maximum spreading diameter (figure 2iii). Zhang  
 83 *et al.* (2022) revealed that also the jump-off is accompanied by a peak in the normal  
 84 reaction force, which was up to then unknown (figure 2,  $F_2(t_2 = 4.63\text{ ms}) \approx 2.3\text{ mN}$   
 85 for the second force peak amplitude—at time  $t_2$  after impact). The second peak in the  
 86 force also coincides with the formation of a Worthington jet, a narrow upward jet of  
 87 liquid that can form due to flow focusing by the retracting drop (figure 2iv-vi). Under  
 88 certain conditions ( $We \approx 9$ ), this peak can be even more pronounced than the first. This  
 89 discovery is critical for superhydrophobicity which is volatile and can fail due to external  
 90 disturbances such as pressure (Lafuma & Quéré 2003; Callies & Quéré 2005; Sbragaglia  
 91 *et al.* 2007; Li *et al.* 2017), evaporation (Tsai *et al.* 2010; Chen *et al.* 2012; Papadopoulos  
 92 *et al.* 2013), mechanical vibration (Bormashenko *et al.* 2007), or the impact forces of  
 93 prior droplets (Bartolo *et al.* 2006a).

94 In contrast to our prior study Zhang *et al.* (2022), which fixed the Ohnesorge number  
 95 to that of a 2 mm diameter water drop ( $Oh = 0.0025$ ), our present investigation reported  
 96 in this paper explores a broader parameter space. We systematically and independently  
 97 vary the Weber and Ohnesorge numbers, extending the range of  $Oh$  to as high as 100.  
 98 This comprehensive approach enables us to develop new scaling laws and provides a  
 99 more unified understanding of the forces involved in drop impact problems. Our findings  
 100 are particularly relevant for applications with varying viscosities and impact velocities  
 101 (figure 1).

102 The structure of this paper is as follows: §2 briefly describes the experimental and  
 103 numerical methods. §3 and §4 offer detailed analyses of the first and second peaks,  
 104 respectively, focusing on their relationships with the Weber number ( $We$ ) and the  
 105 Ohnesorge number ( $Oh$ ). Conclusions and perspectives for future research are presented  
 106 in Section 5.

glycerol (wt %)	$\rho_d$ (kg/m <sup>3</sup> )	$\eta_d$ (mPa.s)	$\gamma$ (mN/m)
0	1000	1	72
50	1124	5	61
63	1158	10	61
74	1188	25.3	61
80	1200	45.4	61
85	1220	80.2	61

TABLE 1. Properties of the water-glycerol mixtures used in the experiments.  $\rho_d$  and  $\eta_d$  are the density and viscosity of the drop, respectively and  $\gamma$  denotes the liquid-air surface tension coefficient. These properties are calculated using the protocol provided in [Cheng \(2008\); Volk & Kähler \(2018\)](#).

## 107 2. Methods

### 108 2.1. Experimental method

109 In the experimental setup, shown schematically in figure 1(a), a liquid drop impacts a  
110 superhydrophobic substrate. For water drops, such a surface is coated with silanized silica  
111 nanobeads with a diameter of 20 nm (Glaco Mirror Coat Zero; Soft99) resulting in the  
112 advancing and receding contact angles of  $167 \pm 2^\circ$  and  $154 \pm 2^\circ$ , respectively ([Gauthier  
113 et al. 2015; Li et al. 2017](#)). On the other hand, for viscous aqueous glycerin drops,  
114 the upper surface is coated with an acetone solution of hydrophobic beads (Ultra ever  
115 Dry, Ultratech International, a typical bead size of 20 nm), resulting in the advancing  
116 and receding contact angles of  $166 \pm 4^\circ$  and  $159 \pm 2^\circ$ , respectively ([Jha et al. 2020](#)).  
117 The properties of the impacting drop are controlled using water-glycerol mixtures with  
118 viscosities  $\eta_d$  varying by almost two orders of magnitude, from 1 mPas to 80.2 mPas,  
119 yet maintaining a fairly constant surface tension  $\gamma$  and density  $\rho_d$  around 61 mN/m  
120 and 1000 kg/m<sup>3</sup>, respectively ([Cheng 2008; Volk & Kähler 2018; Jha et al. 2020](#)). Using  
121 other liquids like silicone oil could allow for a wider viscosity variation if used with  
122 a superamphiphobic substrate ([Deng et al. 2012](#)). The drop diameter  $D_0$  is controlled  
123 between 2.05 mm and 2.76 mm by pushing it through a calibrated needle. Throughout this  
124 work, we use drops with diameter  $2.54 \pm 0.02$  mm unless otherwise stated. Consequently,  
125 changing the viscosity of the drop determines the Ohnesorge number ( $Oh$ , see (1.2)).  
126 The Weber number ( $We$ , see (1.1)) is set using the impact velocity  $V_0$  varying between  
127 0.38 m/s and 2.96 m/s by changing the release height of the drops above the substrate.  
128 All experiments are conducted at ambient pressure and temperature. The impact force  
129 is directly measured using a high-precision piezoelectric force transducer (Kistler 9215A)  
130 with a resolution of 0.5 mN. During these measurements, the high-frequency vibrations  
131 induced by the measurement system and the surrounding noise are spectrally removed  
132 using a low pass filter with a cut-off frequency of 5 kHz, following the procedure in [Li et al.  
133 \(2014\); Zhang et al. \(2017\); Gordillo et al. \(2018\); Mitchell et al. \(2019\)](#). The experiment  
134 also employs a high-speed camera (Photron Fastcam Nova S12) synchronized at 10,000  
135 fps with a shutter speed 1/20,000 s. [Throughout the manuscript, the error bars account  
136 for repeated trials and are visible if they are larger than the marker size.](#) We refer the  
137 readers to the supplementary material of [Zhang et al. \(2022\)](#) and appendix A for further  
138 details of the experimental setup and error characterization of the dimensionless control  
139 parameters, respectively.

140                   2.2. Numerical framework

141                   In the direct numerical simulations (DNS) employed for this study, the continuity and  
 142                   the momentum equations take the form

$$\nabla \cdot \mathbf{v} = 0 \quad (2.1)$$

143                   and

$$\frac{\partial \mathbf{v}}{\partial t} + \nabla \cdot (\mathbf{v} \mathbf{v}) = \frac{1}{\rho} (-\nabla p + \nabla \cdot (2\eta \mathcal{D}) + \mathbf{f}_\gamma) + \mathbf{g}, \quad (2.2)$$

144                   respectively. Here,  $\mathbf{v}$  is the velocity field,  $t$  is time,  $p$  is pressure, and  $\mathbf{g}$  is acceleration  
 145                   due to gravity. We use the free software program *Basilisk C* that employs the well-  
 146                   balanced geometric volume of fluid (VoF) method (Popinet 2009, 2018). The VoF tracer  
 147                    $\Psi$  delineates the interface between the drop (subscript  $d$ ,  $\psi = 1$ ) and air (subscript  $a$ ,  
 148                    $\psi = 0$ ), introducing a singular force  $\mathbf{f}_\gamma \approx \gamma\kappa\nabla\Psi$  ( $\kappa$  denotes interfacial curvature, see  
 149                   Brackbill *et al.* 1992) to respect the dynamic boundary condition at the interface. This  
 150                   VoF tracer sets the material properties such that density  $\rho$  and viscosity  $\eta$  are given by

$$\rho = \rho_a + (\rho_d - \rho_a)\Psi \quad (2.3)$$

151                   and

$$\eta = \eta_a + (\eta_d - \eta_a)\Psi, \quad (2.4)$$

152                   respectively. This VoF field is advected with the flow, following the equation

$$\frac{\partial \Psi}{\partial t} + \nabla \cdot (\mathbf{v}\Psi) = 0. \quad (2.5)$$

153                   Lastly, we calculate the normal reaction force  $\mathbf{F}(t)$  by integrating the pressure field  $p$  at  
 154                   the substrate,

$$\mathbf{F}(t) = \left( \int_{\mathcal{A}} (p - p_0) d\mathcal{A} \right) \hat{\mathbf{z}}, \quad (2.6)$$

155                   where,  $p_0$ ,  $d\mathcal{A}$ , and  $\hat{\mathbf{z}}$  are the ambient pressure, substrate area element, and the unit  
 156                   vector normal to the substrate, respectively.

157                   We leverage the axial symmetry of the drop impact (figure 1a). This axial symmetry  
 158                   breaks at large  $We$  ( $\geq 100$  for water drops and even larger Weber number for more  
 159                   viscous drops), owing to destabilization by the surrounding gas after splashing (Xu *et al.*  
 160                   2005; Eggers *et al.* 2010; Driscoll & Nagel 2011; Riboux & Gordillo 2014; Josserand &  
 161                   Thoroddsen 2016; Zhang *et al.* 2022). To solve the governing equations (2.1)–(2.5), the  
 162                   velocity field  $\mathbf{v}$  and time  $t$  are normalized by the inertio-capillary scales,  $V_\gamma = \sqrt{\gamma/\rho_d D_0}$   
 163                   and  $\tau_\gamma = \sqrt{\rho_d D_0^3/\gamma}$ , respectively. Furthermore, the pressure is normalized using the  
 164                   capillary pressure scale  $p_\gamma = \gamma/D_0$ . In such a conceptualization,  $Oh$  and  $We$  described in  
 165                   §1 uniquely determine the system. The Ohnesorge number based on air viscosity  $Oh_a =$   
 166                    $(\eta_a/\eta_d)Oh$  and air-drop density ratio  $\rho_a/\rho_d$  are fixed at  $10^{-5}$  and  $10^{-3}$ , respectively  
 167                   to minimize the influence of the surrounding medium on the impact forces. Lastly, we  
 168                   keep the Bond number ( $Bo$ , see (1.3)) fixed at 1 throughout the manuscript. In our

system, the relevance of gravity is characterized by the dimensionless Froude number  $Fr = V_0^2/gD_0 = We/Bo$  comparing inertia with gravity. Throughout this manuscript,  $Fr > 1$  and gravity's role is sub-dominant compared to inertia (for detailed discussion, see appendix B). The substrate is modeled as a no-slip and non-penetrable wall, whereas vanishing stress and pressure are applied at the remaining boundaries to mimic outflow conditions for the surrounding air. The domain boundaries are far enough from the drop not to influence its impact process ( $\mathcal{L}_{\max} \gg D_0$ ,  $\mathcal{L}_{\max} = 8R$  in the worst case). At  $t = 0$ , in our simulations, we release a spherical drop (see appendix C) whose south pole is 0.05 $D_0$  away from the substrate and is falling with a velocity  $V_0$ . The simulations utilize adaptive mesh refinement to finely resolve the velocity, viscous dissipation, and the VoF tracer fields. A minimum grid size  $\Delta = D_0/2048$  is used for this study.

To ensure a perfectly non-wetting surface, we impose a thin air layer (minimum thickness  $\sim \Delta/2$ ) between the drop and the substrate. This air layer prevents direct contact between the liquid and solid (Kolinski *et al.* 2014; Sprittles 2024), effectively mimicking a perfectly non-wetting surface. The presence of this air layer is crucial for capturing the dynamics of drop impact on superhydrophobic surfaces, as it allows for the formation of an air cushion that can significantly affect the spreading and rebound behavior of the drop (Ramírez-Soto *et al.* 2020; Sanjay *et al.* 2023a). While this approach does not fully resolve the microscopic dynamics within the air layer itself, such as the high-velocity gradients and viscous dissipation inside the gas film once it thins below a critical size ( $\sim 10\Delta$ ), it has been shown to accurately capture the macroscopic behavior of drop impact in the parameter range of interest (Ramírez-Soto *et al.* 2020; Sanjay *et al.* 2023b; Alventosa *et al.* 2023a; García-Geijo *et al.* 2024). We refer the readers to Sanjay (2022) for discussions about this “precursor”, air film method and to Popinet & collaborators (2013–2023); Sanjay (2023); Zhang *et al.* (2022) for details on the numerical framework.

### 3. Anatomy of the first impact force peak

This section elucidates the anatomy of the first impact force peak and its relationship with the Weber  $We$  and Ohnesorge  $Oh$  numbers, first for the inertial limit (§3.1,  $Oh \ll 1$ ) and then for the viscous asymptote (§3.2,  $Oh \gg 1$ ). The results of this section are summarized in figure 3 that shows an excellent agreement between experiments and simulations without any free parameters.

#### 3.1. Low Ohnesorge number impacts

For low  $Oh$  and large  $We$ , inertial force and time scales dictate the drop impact dynamics (figures 3 and 4). As the drop falls on a substrate, the part of the drop immediately in contact with the substrate stops moving, whereas the top of the drop still falls with the impact velocity (figure 4, from  $t = t_1/4$  until  $t = t_1$ ). Consequently, momentum conservation implies

$$F_1 \sim V_0 \frac{dm}{dt}, \quad (3.1)$$

where the mass flux  $dm/dt \sim \rho_d V_0 D_0^2$  (Soto *et al.* 2014; Zhang *et al.* 2022). As a result, the first peak amplitude scales with the inertial pressure force (figure 3a)

$$F_1 \sim F_\rho, \text{ where } F_\rho = \rho_d V_0^2 D_0^2, \quad (3.2)$$

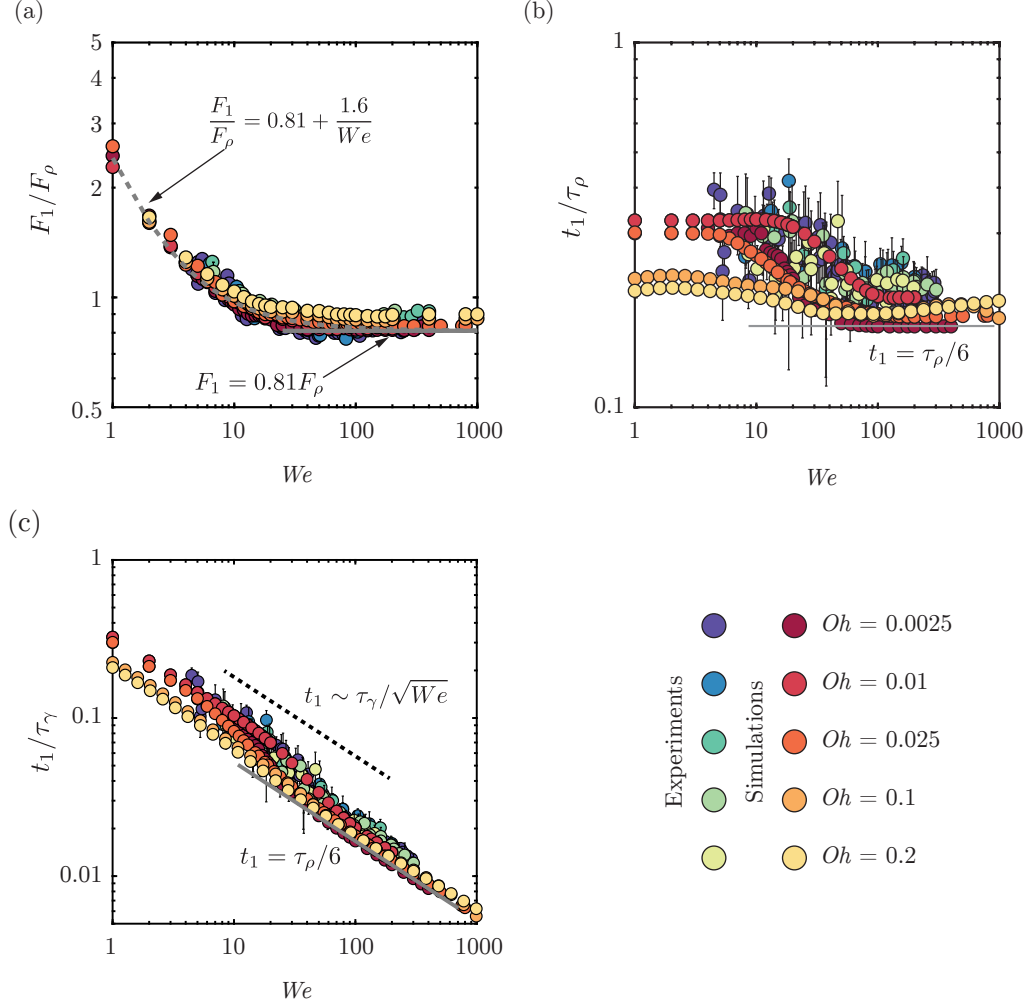


FIGURE 3. Anatomy of the first impact force peak amplitude at low  $Oh$  in between 0.0025 and 0.2, see color legend:  $We$  dependence of the (a) magnitude  $F_1$  normalized by the inertial force scale  $F_\rho = \rho_d V_0^2 D_0^2$  and time  $t_1$  to reach the first force peak amplitude normalized by (b) the inertial timescale  $\tau_\rho = D_0/V_0$  and (c) the inertia-capillary time scale  $\tau_\gamma = \sqrt{\rho_d D_0^3/\gamma}$ .

209 for high Weber numbers ( $We > 30$ ,  $F_1 \approx 0.81F_\rho$ ). Furthermore, the time  $t_1$  to reach  $F_1$   
210 follows

$$t_1 \sim \frac{D_0}{V_0} = \tau_\rho, \quad (3.3)$$

211 where,  $\tau_\rho$  is the inertial timescale. The relation between equations (3.2) and (3.3) is  
212 apparent from the momentum conservation which implies that the impulse of the first  
213 force peak is equal to the momentum of the impacting drop, i.e.,  $F_1 t_1 \sim \rho_d V_0 D_0^3 = F_\rho \tau_\rho$   
214 (see Gordillo *et al.* 2018, Zhang *et al.* 2022, and figures 3b,c). These scaling laws depend  
215 only on the inertial shock at impact and are wettability-independent (Zhang *et al.* 2017;  
216 Gordillo *et al.* 2018; Zhang *et al.* 2022). For details of the scaling law, including the

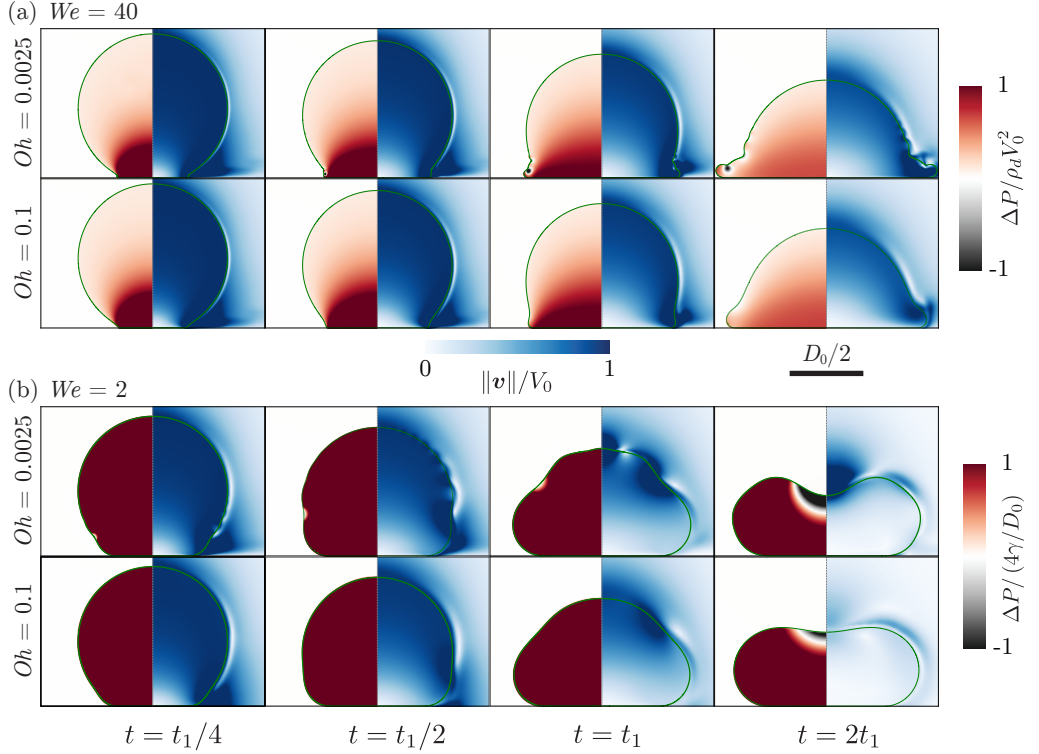


FIGURE 4. Direct numerical simulations snapshots illustrating the drop impact dynamics for  $We =$  (a) 40 and (b) 2. The left-hand side of each numerical snapshot shows the pressure normalized by (a) the inertial pressure scale  $\rho_d V_0^2$  and (b) the capillary pressure scale  $\gamma / D_0$ . The right-hand side shows the velocity field magnitude normalized by the impact velocity  $V_0$ .

prefactors, we refer the readers to [Philippi et al. \(2016\)](#); [Gordillo et al. \(2018\)](#); [Cheng et al. \(2022\)](#).

[Figure 3](#) further illustrates that this inertial asymptote is insensitive to viscosity variations up to 100-fold as  $F_1 \sim F_\rho$  and  $t_1 \sim \tau_\rho$  for  $0.0025 < Oh < 0.2$ . However, deviations from the inertial force and time scales are apparent for  $We < 30$  ([figure 3](#)), a phenomenon also reported in earlier work ([Soto et al. 2014](#); [Zhang et al. 2022](#)). In these instances, inertia does not act as the sole governing force but instead complements surface tension, which dictates the pressure inside the drop ( $p \sim \gamma / D_0$  throughout the drop for  $We \lesssim 1$ , [figure 4b](#)). [Zhang et al. \(2022\)](#) proposed an empirical functional dependence as

$$F_1 = \left( \alpha_1 \rho_d V_0^2 + \alpha_2 \frac{\gamma}{D_0} \right) D_0^2, \quad (3.4)$$

based on dimensional analysis, with  $\alpha_1$  and  $\alpha_2$  as free parameters which were determined to be approximately 1.6 and 0.81, respectively for water ( $Oh = 0.0025$ ). These coefficients only deviate marginally in the current work despite the significant increase in  $Oh$  as compared to previous works ([Cheng et al. 2022](#); [Zhang et al. 2022](#)). This consistency underscores the invariance of the pressure field inside the drop to an increase in  $Oh$  (close to the impact region, [figure 4a](#) and throughout the drop, [figure 4b](#)).

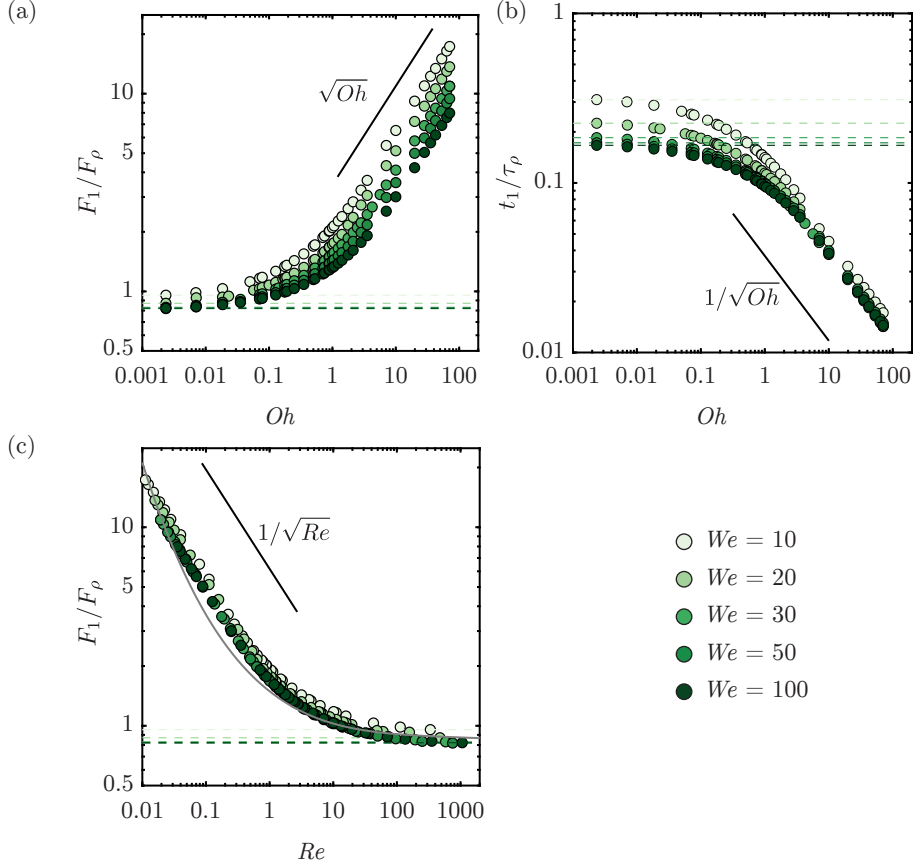


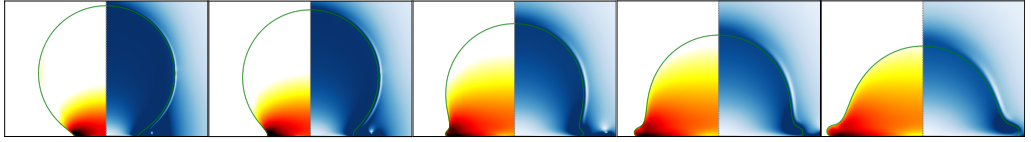
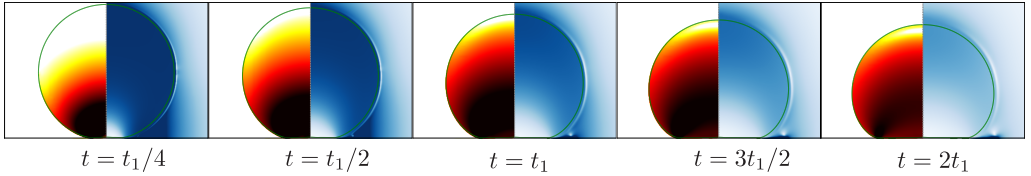
FIGURE 5. Anatomy of the first impact force peak amplitude for viscous impacts from our numerical simulations: the  $Oh$  dependence of (a) the magnitude  $F_1$  normalized by the inertial force scale  $\rho_d V_0^2 D_0^2$  and (b) the time  $t_1$  to reach the first force peak amplitude normalized by inertial timescale  $\tau_\rho = D_0/V_0$ . (c) The  $Re$  dependence of the magnitude  $F_1$  normalized by the inertial force scale  $\rho_d V_0^2 D_0^2$  as compared to the (implicit) theoretical calculation of Gordillo *et al.* (2018). The black line corresponds to the scaling relationship described in §3.2. The Weber number is color-coded.

### 3.2. Large Ohnesorge number impacts

Figure 5 reaffirms the findings of §3.1 for low  $Oh$  that the first impact peak amplitude  $F_1$  and the time to reach this peak amplitude  $t_1$  scale with  $F_\rho$  and  $\tau_\rho$ , respectively. As the Ohnesorge number increases further, the first impact force peak amplitude normalized with  $F_\rho$  begins to increase, indicating a transition around  $Oh \approx 0.1$ , where viscosity starts to play a significant role. At large  $Oh$ , we observe the scaling relationship (figure 5a)

$$F_1 \sim F_\rho \sqrt{Oh}. \quad (3.5)$$

The drop's momentum is still  $\rho_d V_0 D_0^3$  which must be balanced by the impulse from the substrate,  $F_1 t_1$  (see §3.1, Gordillo *et al.* 2018, Zhang *et al.* 2022, and figure 5b). Consequently, the time  $t_1$  follows

(a)  $Oh = 0.05$ (b)  $Oh = 0.5$ (c)  $Oh = 5$ 

$t = t_1/4 \quad t = t_1/2 \quad t = t_1 \quad t = 3t_1/2 \quad t = 2t_1$

$$\begin{array}{c} -3 \quad \log_{10} (\tilde{\xi}_\eta) \quad 0.5 \\ \hline \end{array} \quad \begin{array}{c} D_0/2 \\ \hline 0 \quad \|v\|/V_0 \quad 1 \end{array}$$

FIGURE 6. Direct numerical simulations snapshots illustrating the drop impact dynamics for  $We = 100$  and  $Oh =$  (a)  $0.05$ , (b)  $0.5$ , and (c)  $5$ . The left-hand side of each numerical snapshot shows the viscous dissipation function  $\tilde{\xi}_\eta$  normalized by the inertial scale  $\rho_d V_0^3 / D_0$ . The right-hand side shows the velocity field magnitude normalized by the impact velocity  $V_0$ .

$$t_1 \sim \frac{\tau_\rho}{\sqrt{Oh}}. \quad (3.6)$$

Figure 5 further shows that these scaling laws are weakly dependent on the Weber number, as viscous dissipation consumes the entire initial kinetic energy of the impacting drop (figure 6). Once again, we stress that using the water-glycerol mixtures limits the range of  $Oh$  that we can probe experimentally. We further note that the first peak is robust and does not depend on the wettability of the substrate. Consequently, to compare with the existing data such as those in Cheng *et al.* (2022) with different liquids to cover a wider range of liquid viscosities and to account for the apparent  $We$ -dependence, we plot  $F_1$  compensated with  $F_\rho$  against the impact Reynolds number  $Re \equiv \sqrt{We}/Oh = V_0 D_0 / \nu_d$ . For the low  $Re$  regime, such a plot allows us to describe the  $We$  dependence on the prefactor more effectively, as illustrated in figure 5(c). However, it is important to note that some scatter is still observed at high  $Re$  values, which can be attributed to the  $We$  dependence of the impact force peak amplitude. This lack of a pure scaling behavior demonstrates how the interplay between kinetic energy and viscous dissipation within the drop dictates the functional dependence of the maximum impact force on  $Oh$ .

To systematically elucidate these scaling behaviors in the limit of small  $Re$ , we need to find the typical scales for the rate of change of kinetic energy and that of the rate of viscous dissipation for the drop impact system. First, we can readily define an average rate of viscous dissipation per unit mass as

$$\bar{\varepsilon} \sim \frac{1}{\tau_\rho} \frac{1}{D_0^3} \int_0^{\tau_\rho} \int_{\Omega} \nu_d (\mathcal{D} : \mathcal{D}) d\Omega dt, \quad (3.7)$$

where  $\nu_d$  is the kinematic viscosity of the drop and  $d\Omega$  is the volume element where dissipation occurs. Notice that  $\bar{\varepsilon}$  has the dimensions of  $V_0^3/D_0$ , i.e., length squared over time cubed or velocity squared over time, as it should be for dissipation rate of energy per unit mass. We can estimate  $\Omega = D_{\text{foot}}^2 l_\nu$  (figure 6), where  $D_{\text{foot}}$  is the drop's foot diameter in contact with the substrate and  $l_\nu$  is the viscous boundary layer thickness. This boundary layer marks the region of strong velocity gradients ( $\sim V_0/l_\nu$ ) analogous to the Mirels (1955) shockwave-induced boundary layer. For details, we refer the authors to Schlichting (1968); Schroll *et al.* (2010); Philippi *et al.* (2016). Consequently, the viscous dissipation rate scales as

$$\bar{\varepsilon} \sim \frac{1}{\tau_\rho D_0^3} \int_0^{\tau_\rho} \nu_d \left( \frac{V_0}{l_\nu} \right)^2 D_{\text{foot}}^2 l_\nu dt. \quad (3.8)$$

To calculate  $D_{\text{foot}}$ , we assume that the drop maintains a spherical cap shape throughout the impact (figure 6). To calculate the distance the drop would have traveled if there were no substrate, we use the relation  $d \sim V_0 t$ . Simple geometric arguments allow us to determine the relation between the foot diameter and this distance,  $D_{\text{foot}} \sim \sqrt{D_0 d}$  (Lesser 1981; Mandre *et al.* 2009; Zheng *et al.* 2021; Bilotto *et al.* 2023; Bertin 2023). Interestingly, this scaling behavior is similar to the inertial limit (Wagner 1932; Bouwhuis *et al.* 2012; Philippi *et al.* 2016; Gordillo *et al.* 2019) as discussed by Langley *et al.* (2017); Bilotto *et al.* (2023). Furthermore, the viscous boundary layer  $l_\nu$  can be approximated using  $\sqrt{\nu_d t}$  (Mirels 1955; Eggers *et al.* 2010; Philippi *et al.* 2016). Filling these in (3.8), we get

$$\bar{\varepsilon} \sim \frac{1}{\tau_\rho D_0^2} \int_0^{\tau_\rho} \sqrt{\nu_d} V_0^3 \sqrt{t} dt, \quad (3.9)$$

which on integration gives

$$\bar{\varepsilon} \sim \sqrt{\nu_d \tau_\rho} V_0^3 / D_0^2, \quad (3.10)$$

where  $\tau_\rho$  is the inertial time scale. Here, we assume that for highly viscous drops, all energy is dissipated within a fraction of  $\tau_\rho$ . Filling in (3.10) and normalizing  $\bar{\varepsilon}$  with the inertial scales  $V_0^3/D_0$ ,

$$\frac{\bar{\varepsilon}}{V_0^3/D_0} \sim \sqrt{\frac{\nu_d \tau_\rho}{D_0^2}} = \frac{1}{\sqrt{Re}} = \left( \frac{Oh}{\sqrt{We}} \right)^{1/2}. \quad (3.11)$$

Next, the kinetic energy of the falling drop is given by

$$\dot{K}(t) \equiv \frac{dK(t)}{dt} \sim \rho_d D_0^3 \bar{\varepsilon}, \quad \text{where } K(t) = \frac{1}{2} m (V(t))^2, \quad (3.12)$$

and  $V(t)$  is the drop's center of mass velocity. The left-hand side of (3.12) can be written as

$$\dot{K}(t) = mV(t) \frac{dV(t)}{dt} = F(t)V(t). \quad (3.13)$$

285 In equation (3.13),  $F(t)$  and  $V(t)$  scale with the first impact force peak amplitude  $F_1$   
 286 and the impact velocity  $V_0$ , respectively, giving the typical scale of the rate of change of  
 287 kinetic energy as

$$\dot{K}^* \sim F_1 V_0. \quad (3.14)$$

288 We stress that (3.14) states that the rate of change of kinetic energy is equal to the power  
 289 of the normal reaction force, an observation already made by [Wagner \(1932\)](#) and [Philippi  
et al. \(2016\)](#) in the context of impact problems. Lastly, at large  $Oh$ , viscous dissipation  
 290 enervates kinetic energy completely giving (figure 6c, also see: [Philippi et al. \(2016\)](#) and  
 291 [Wildeman et al. \(2016\)](#)),

$$\dot{K}^* \sim F_1 V_0 \sim \rho_d D_0^3 \bar{\varepsilon} \quad (3.15)$$

293 Additionally, we use the inertial scales to non-dimensionalize (3.15) and fill in (3.11),  
 294 giving

$$\frac{F}{F_\rho} \sim \frac{\bar{\varepsilon}}{V_0^3/D_0} \sim \frac{1}{\sqrt{Re}} = \left( \frac{Oh}{\sqrt{We}} \right)^{1/2} \quad (3.16)$$

295 and using  $F_1 t_1 \sim \rho_d V_0 D_0^3 = F_\rho \tau_\rho$ ,

$$\frac{t_1}{\tau_\rho} \sim \left( \frac{\sqrt{We}}{Oh} \right)^{1/2}. \quad (3.17)$$

296 In summary, we use energy and momentum invariance to elucidate the parameter  
 297 dependencies of the impact force as illustrated in figure 5. The scaling arguments  
 298 capture the dominant force balance during the impact process, considering the relative  
 299 importance of inertial, capillary, and viscous forces. As the dimensionless viscosity of  
 300 impacting drops increases, the lack of surface deformation increases the normal reaction  
 301 force (3.16). Further, the invariance of incoming drop momentum implies that this  
 302 increase in normal reaction force occurs on a shorter timescale (3.17).

#### 303 4. Anatomy of the second impact force peak

304 This section delves into the anatomy of the second impact force peak amplitude  $F_2$  as a  
 305 function of the Weber  $We$  and Ohnesorge  $Oh$  numbers, summarized in figure 7. We once  
 306 again note the remarkable agreement between experiments and numerical simulations in  
 307 this figure.

308 Similar to the mechanism leading to the formation of the first peak (§3), also the  
 309 mechanism for the formation of this second peak is momentum conservation. As the  
 310 drop takes off the surface, it applies a force on the substrate. As noted in §1 and [Zhang  
et al. \(2022\)](#), this force also coincides with the formation of a Worthington jet (figure 2iv-  
 311 vi). The time  $t_2$  at which the second peak is observed scales with the inertio-capillary  
 312 timescale and is insensitive to  $We$  and  $Oh$  (figure 7b,c). Once again, we invoke the analogy  
 313

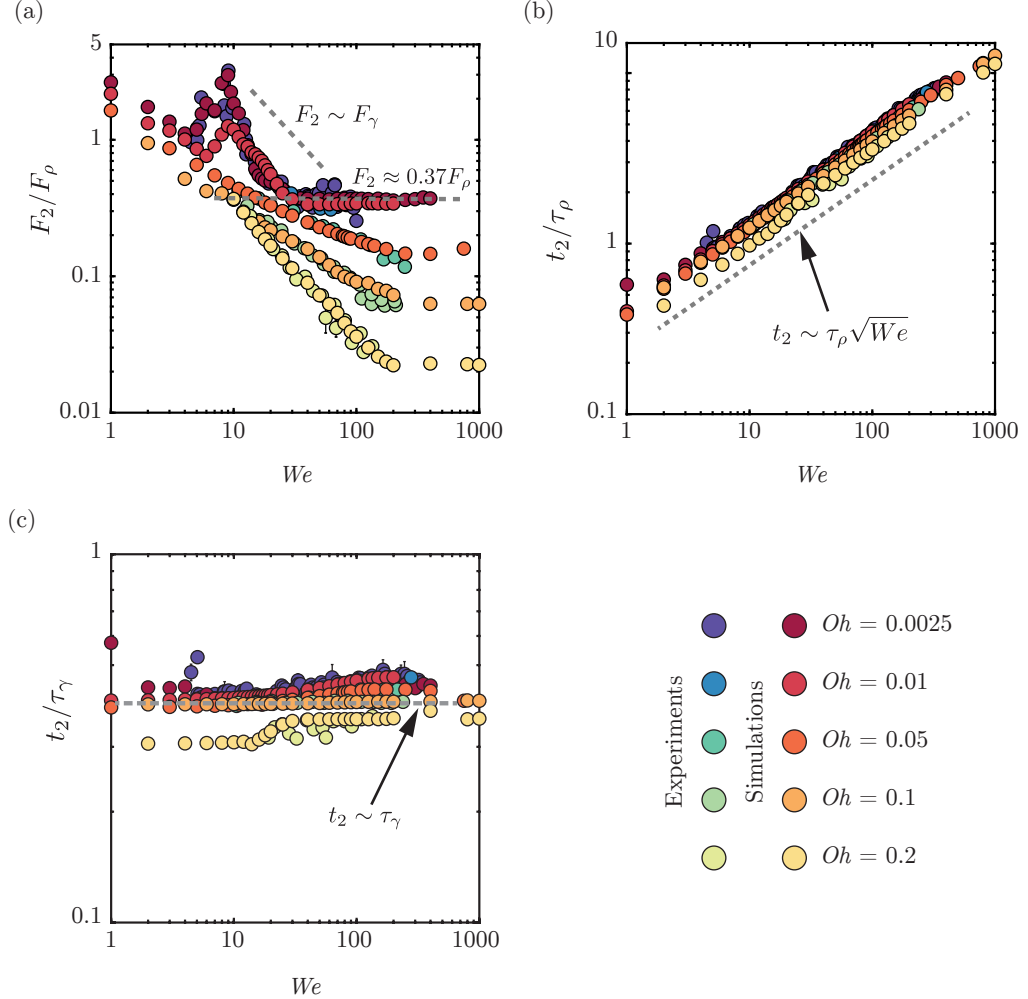


FIGURE 7. Anatomy of the second impact force peak amplitude:  $We$  dependence of the (a) magnitude  $F_2$  normalized by the inertial force scale  $F_\rho = \rho_d V_0^2 D_0^2$  and time  $t_2$  to reach the second force peak amplitude normalized by (b) the inertio-capillary time scale  $\tau_\gamma = \sqrt{\rho_d D_0^3 / \gamma}$  and (c) inertial timescale  $\tau_\rho = D_0 / V_0$ .

314 between drop oscillation and drop impact to explain this behavior (Richard *et al.* 2002;  
 315 Chevy *et al.* 2012). At the time instant  $t_2 \approx 0.44\tau_\gamma$ , the drop's internal motion undergoes  
 316 a transition from a predominantly radial flow to a vertical one due to the formation of  
 317 the Worthington jet (Chantelot 2018; Zhang *et al.* 2022). Figure 8 exemplifies this jet in  
 318 the  $Oh - We$  parameter space, which is intricately related to the second peak in the drop  
 319 impact force. For low  $Oh$  and large  $We$ , the drop retraction follows a modified Taylor-  
 320 Culick dynamics (Bartolo *et al.* 2005; Eggers *et al.* 2010; Sanjay *et al.* 2022). As  $We$  is  
 321 increased, the jet gets thinner but faster, maintaining a constant momentum flux  $\rho_d V_j^2 d_j^2$ ,  
 322 where  $V_j$  and  $d_j$  are the jet's velocity and diameter, respectively (figure 8, Zhang *et al.*  
 323 2022). This invariance leads to the observed scaling  $F_2 \sim F_\rho$  in this regime ( $F_2 \approx 0.37F_\rho$   
 324 for  $We \geq 30, Oh \leq 0.01$ ).

325 Furthermore, the low  $We$  and  $Oh$  regime relies entirely on capillary pressure (figure 4).

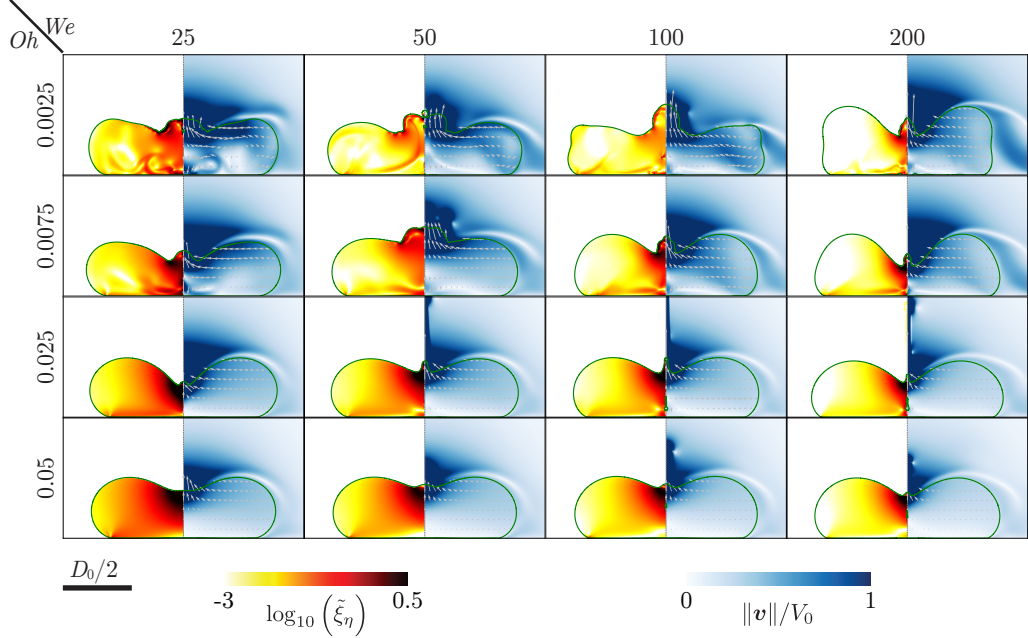


FIGURE 8. Direct numerical simulations snapshots illustrating the influence of  $We$  and  $Oh$  on the inception of the Worthington jet. All these snapshots are taken at the instant when the second peak appears in the temporal evolution of the normal reaction force ( $t = t_2$ ). The left-hand side of each numerical snapshot shows the viscous dissipation function  $\xi_\eta$  normalized by the inertial scale  $\rho_d V_0^3 / D_0$ . The right-hand side shows the velocity field magnitude normalized by the impact velocity  $V_0$ . The gray velocity vectors are plotted in the center of mass reference frame of the drop to clearly elucidate the internal flow.

Subsequently,  $F_2 \sim F_\gamma = \gamma D_0$  for  $Oh < 0.01$  and  $We < 30$  (figure 7). This flow focusing (figure 8) is most efficient for  $We = 9$  (figure 9a,  $t_2/2 < t < t_2$ , Renard *et al.* 2003; Bartolo *et al.* 2006b) where the capillary resonance leads to a thin-fast jet, accompanied by a bubble entrainment, reminiscent of the hydrodynamic singularity (figure 9, Zhang *et al.* 2022; Sanjay *et al.* 2021). The characteristic feature of this converging flow is a higher magnitude of  $F_2$  compared to  $F_1$  (figure 7).

However, this singular jet regime is very narrow in the  $Oh - We$  phase space. Figure 9b shows two cases for water drops ( $Oh = 0.0025$ ) at different  $We$  (5 and 12 for figures 9b-i and b-ii, respectively). Bubble entrainment does not occur in either of these cases. Consequently, the maximum force amplitude diminishes for these two cases (figure 7). Nonetheless, these cases are still associated with high local viscous dissipation near the axis of symmetry owing to the singular nature of the flow. Another mechanism to inhibit this singular Worthington jet is viscous dissipation in the bulk. As the Ohnesorge number increases, this singular jet formation disappears ( $Oh = 0.005$ , figure 9c-i), significantly reducing the second peak of the impact force. For even higher viscosities, the drop no longer exhibits the sharp, focused jet formation seen at lower viscosities, and the second peak in the force is notably diminished ( $Oh = 0.05$ , figure 9c-ii).

Lastly, as  $Oh$  increases, bulk dissipation becomes dominant (apparent from increasing  $Oh$  at fixed  $We$  in figure 8) and can entirely inhibit drop bouncing. Recently, Jha *et al.* (2020); Sanjay *et al.* (2023a) showed that there exists a critical  $Oh$ , two orders of magnitude higher than that of a 2 mm diameter water drop, beyond which drops do not bounce either, irrespective of their impact velocity. Consequently, the second peak

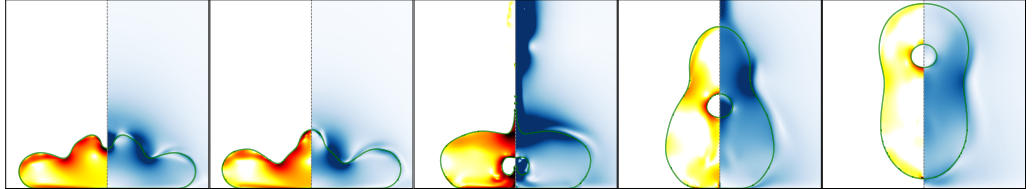
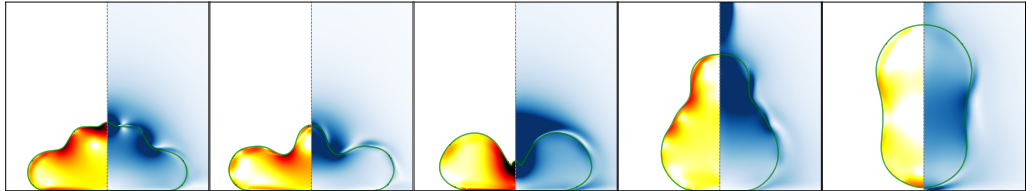
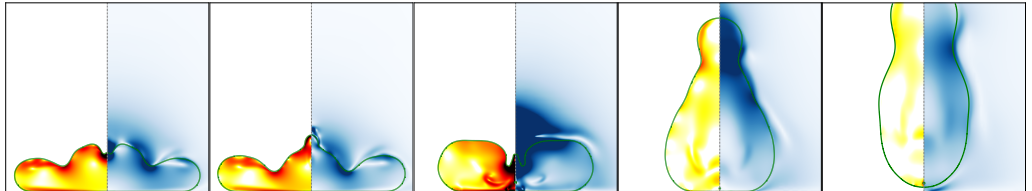
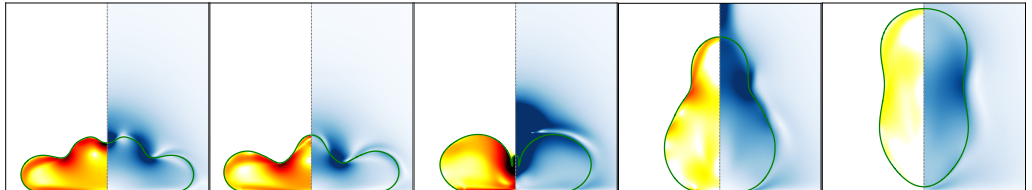
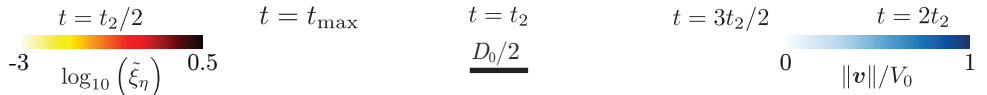
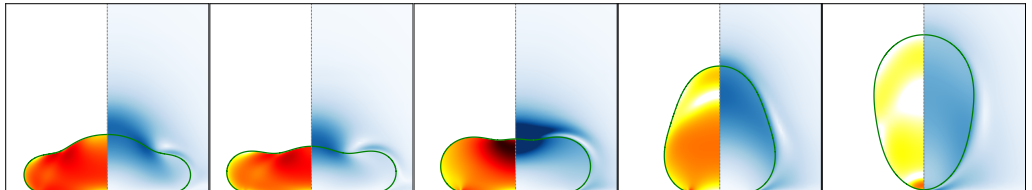
(a)  $We = 9, Oh = 0.0025$ (b)  $Oh = 0.0025$ (i)  $We = 5$ (ii)  $We = 12$ (c)  $We = 9$ (i)  $Oh = 0.005$ (ii)  $Oh = 0.05$ 

FIGURE 9. Direct numerical simulations snapshots illustrating the influence of  $We$  and  $Oh$  on the singular Worthington jet. (a)  $(We, Oh) = (9, 0.0025)$ , (b)  $Oh = 0.0025$  with  $We =$  (i) 5 and (ii) 12, and (c)  $We = 9$  with  $Oh =$  (i) 0.005 and (ii)  $Oh = 0.05$ . The left-hand side of each numerical snapshot shows the viscous dissipation function  $\xi_\eta$  normalized by inertial scale  $\rho_d V_0^3 / D_0$ . The right-hand side shows the velocity field magnitude normalized by the impact velocity  $V_0$ .

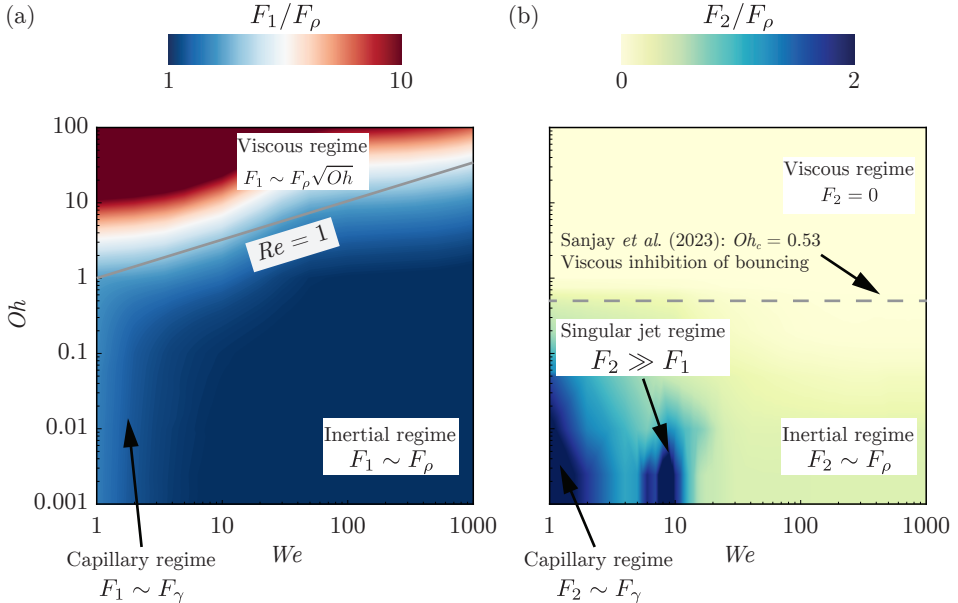


FIGURE 10. Regime map in terms of the drop Ohnesorge number  $Oh$  and the impact Weber number  $We$  to summarize the two peaks in the impact force by showing the different regimes described in this work based on (a) the first peak in the impact force peak amplitude  $F_1$  and (b) the second peak in the impact force peak amplitude  $F_2$ . Both peaks are normalized by the inertial force scale  $F_\rho = \rho_d V_0^2 D_0^2$ . These regime maps are constructed using  $\sim 1500$  simulations in the range  $0.001 \leq Oh \leq 100$  and  $1 \leq We \leq 1000$ . The gray solid line in (a) and dashed line in (b) mark the inertial-viscous transition ( $Re = 1$ ) and the bouncing-no-bouncing transition ( $Oh_c = 0.53$  for  $Bo = 1$ , see [Sanjay et al. \(2023a\)](#)), respectively.

in the impact force diminishes for larger  $Oh$ , which explains the monotonic decrease of the amplitude  $F_2$  observed in figure 7 for  $We > 30, Oh > 0.01$ .

## 5. Conclusion and outlook

In this work, we study the forces and dissipation encountered during the drop impact process by employing experiments, numerical simulations, and theoretical scaling laws. We vary the two dimensionless control parameters—the Weber ( $We$ : dimensionless impact velocity) and the Ohnesorge number ( $Oh$ : dimensionless viscosity) independently to elucidate the intricate interplay between inertia, viscosity, and surface tension in governing the forces exerted by a liquid drop upon impact on a non-wetting substrate.

For the first impact force peak amplitude  $F_1$ , owing to the momentum balance after the inertial shock at impact, figure 10(a) summarizes the different regimes in the  $Oh$ — $We$  phase space. For low  $Oh$ , inertial forces predominantly dictate the impact dynamics, such that  $F_1$  scales with the inertial force  $F_\rho$  ([Philippi et al. 2016](#); [Gordillo et al. 2018](#); [Mitchell et al. 2019](#); [Cheng et al. 2022](#); [Zhang et al. 2022](#)) and is insensitive to viscosity variations up to 100-fold. As  $Oh$  increases, the viscosity becomes significant, leading to a new scaling law:  $F_1 \sim F_\rho \sqrt{Oh}$ . The paper unravels this viscous scaling behavior by accounting for the loss of initial kinetic energy owing to viscous dissipation inside the drop. Lastly, at low  $We$ , the capillary pressure inside the drop leads to the scaling  $F_1 \sim F_\gamma$  ([Moláček & Bush 2012](#); [Chevy et al. 2012](#)).

The normal reaction force described in this work is responsible for deforming the drop as it spreads onto the substrate, where it stops thanks to surface tension. If the

substrate is non-wetting, it retracts to minimize the surface energy and finally takes off (Richard & Quéré 2000). In this case, the momentum conservation leads to the formation of a Worthington jet and a second peak in the normal reaction force, as summarized in figure 10(b). For low  $Oh$  and high  $We$ , the second force peak amplitude scales with the inertial force ( $F_\rho$ ), following a modified Taylor-Culick dynamics (Eggers *et al.* 2010). In contrast, capillary forces dominate at low  $We$  and low  $Oh$ , leading to a force amplitude scaling of  $F_2 \sim F_\gamma$ . We also identify a narrow regime in the  $Oh - We$  phase space where a singular Worthington jet forms, significantly increasing  $F_2$  (Bartolo *et al.* 2006b; Zhang *et al.* 2022), localized in the parameter space for  $We \approx 9$  and  $Oh < 0.01$ . As  $Oh$  increases, bulk viscous dissipation counteracts this jet formation, diminishing the second peak and ultimately inhibiting drop bouncing.

Our findings have far-reaching implications, not only enriching the fundamental understanding of fluid dynamics of drop impact but also informing practical applications in diverse fields such as inkjet printing, public health, agriculture, and material science where the entire range of  $Oh - We$  phase space is relevant (figures 1b and 10). While this has identified new scaling laws, it also opens avenues for future research. For instance, it would be interesting to use the energy accounting approach to unify the scaling laws for the maximum spreading diameter for arbitrary  $Oh$  (Laan *et al.* 2014; Wildeman *et al.* 2016). Although, the implicit theoretical model summarized in Cheng *et al.* (2022) describes most of data in figure 5, we stress the importance of having a predictive model to determine  $F_1$  for given  $We$  and  $Oh$  (Sanjay & Lohse 2024). The  $We$  influence on the impact force also warrants further exploration, especially in the regime  $We \ll 1$  for arbitrary  $Oh$  (Chevy *et al.* 2012; Moláček & Bush 2012) and drop impact on compliant surfaces (Alventosa *et al.* 2023b; Ma & Huang 2023). Another potential extension of this work is to non-Newtonian fluids (Martouzet *et al.* 2021; Agüero *et al.* 2022; Bertin 2023; Jin *et al.* 2023).

395

**Code availability.** The codes used in the present article are permanently available at Sanjay (2023).

398

**Acknowledgements.** We would like to thank Vincent Bertin for comments on the manuscript. We would also like to thank Andrea Prosperetti, Pierre Chantelot, Devaraj van der Meer, and Uddalok Sen for illuminating discussions.

402

**Funding.** We acknowledge the funding by the ERC Advanced Grant No. 740479-DDD and NWO-Canon grant FIP-II. B.Z and C.L are grateful for the support from National Natural Science Foundation of China (Grant No. 12172189, 11921002, 11902179). This work was carried out on the national e-infrastructure of SURFsara, a subsidiary of SURF cooperation, the collaborative ICT organization for Dutch education and research. This work was sponsored by NWO - Domain Science for the use of supercomputer facilities.

409

**Declaration of Interests.** The authors report no conflict of interest.

411

**Author ORCID.**

V. Sanjay <https://orcid.org/0000-0002-4293-6099>;

B. Zhang <https://orcid.org/0000-0001-8550-2584>;

C. Lv <https://orcid.org/0000-0001-8016-6462>;

415

416 D. Lohse <https://orcid.org/0000-0003-4138-2255>.

417

## 418 Appendix A. Note on the parametric error characterization

419 This appendix outlines the methodology for characterizing experimental errors in quantification of the drop's size and impact velocities which is crucial for accurate calculation  
420 of dimensionless control parameters,  $We$  and  $Oh$ . The drop diameter determination  
421 involved multiple steps. First, we measured the total mass ( $M_{100}$ ) of 100 drops using  
422 an electric balance. From this mass, the drop density, and assuming spherical shape,  
423 we calculated the drop diameter ( $D_0$ ). We repeated this process five times, yielding  
424  $D_{0,1}$  through  $D_{0,5}$ . The average of these measurements provided the final drop diameter  
425 ( $D_0$ ) and its standard error. For impact velocity determination, we extracted data from  
426 experimental high-speed imagery. By tracking the drop center's position in successive  
427 frames prior to substrate contact, and knowing the frame rate, we calculated the impact  
428 velocity. We repeated this process for five trials, obtaining  $V_{0,1}$  through  $V_{0,5}$ . The average  
429 of these values gave the final impact velocity ( $V_0$ ) and its standard error.

430 The standard errors for drop diameters did not exceed 0.13 mm. For drops with  
431 Ohnesorge numbers of 0.0025, 0.0625, and 0.2, the diameters were  $2.05 \pm 0.13$  mm,  $2.52 \pm$   
432 0.11 mm, and  $2.54 \pm 0.09$  mm, respectively. The standard errors for impact velocities did  
433 not exceed 0.02 m/s. For the same  $Oh$  values, the impact velocities were  $1.2 \pm 0.002$  m/s,  
434  $0.97 \pm 0.01$  m/s, and  $0.96 \pm 0.01$  m/s, respectively. The combined errors in  $D_0$  and  $V_0$   
435 resulted in approximately  $\pm 7\%$  error in Weber number  $We$  and  $\pm 3\%$  error in Ohnesorge  
436 number  $Oh$ . Consequently, the horizontal error bars, which relate to errors in the control  
437 parameters, are smaller than the symbol sizes in our figures.

## 438 Appendix B. Role of gravity on drop impact forces

## 439 Appendix C. Role of drop shape on impact forces

440 It is important to note that the drops may not be perfectly spherical and may have  
441 residual oscillations as they are released from the needle and arrive at the substrate.  
442 These oscillations are expected to be more pronounced for cases with small Weber and  
443 Ohnesorge numbers. The exact shape of the drop just before impact can influence the  
444 impact dynamics (Thoraval *et al.* 2013; Yun 2017). However, we suspect that the influence  
445 of these shape variations is captured, at least in part, by the error bars in the experimental  
446 data, which are derived from repeated trials under the same nominal conditions.

## REFERENCES

- 447 AGÜERO, E. A., ALVENTOSA, L. F. L., HARRIS, D. M. & GALEANO-RIOS, C. A. 2022 Impact  
448 of a rigid sphere onto an elastic membrane. *Proc. R. Soc. Lond. A* **478** (2266), 20220340.
- 449 AHMAD, M., SCHATZ, M. & CASEY, M. V. 2013 Experimental investigation of droplet size  
450 influence on low pressure steam turbine blade erosion. *Wear* **303**, 83–86.
- 451 ALVENTOSA, L. F. L., CIMPEANU, R. & HARRIS, D. M. 2023a Inertio-capillary rebound of a  
452 droplet impacting a fluid bath. *J. Fluid Mech.* **958**, A24.
- 453 ALVENTOSA, L. F. L., CIMPEANU, R. & HARRIS, D. M. 2023b Inertio-capillary rebound of a  
454 droplet impacting a fluid bath. *J. Fluid Mech.* **958**, A24.
- 455 AMIRZADEH, B., LOUGHALAM, A., RAESSI, M. & TOOTKABONI, M. 2017 A computational  
456 framework for the analysis of rain-induced erosion in wind turbine blades. *J. Wind Eng.*  
457 *Ind. Aerodyn.* **163**, 33–43.
- 458 BARTOLO, D., BOUAMRIRENE, F., VERNEUIL, E., BUGUIN, A., SILBERZAN, P. & MOULINET,
- 459

- S. 2006a Bouncing or sticky droplets: Impalement transitions on superhydrophobic micropatterned surfaces. *Europhys. Lett.* **74** (2), 299.
- BARTOLO, D., BOUDAOU, A., NARCY, G. & BONN, D. 2007 Dynamics of non-Newtonian droplets. *Phys. Rev. Lett.* **99** (17), 174502.
- BARTOLO, D., JOSSERAND, C. & BONN, D. 2005 Retraction dynamics of aqueous drops upon impact on non-wetting surfaces. *J. Fluid Mech.* **545**, 329–338.
- BARTOLO, D., JOSSERAND, C. & BONN, D. 2006b Singular jets and bubbles in drop impact. *Phys. Rev. Lett.* **96** (12), 124501.
- BERGERON, V., BONN, D., MARTIN, J. Y. & VOVELLE, L. 2000 Controlling droplet deposition with polymer additives. *Nature* **405** (6788), 772–775.
- BERNY, A., POPINET, S., SÉON, T. & DEIKE, L. 2021 Statistics of jet drop production. *Geophys. Res. Lett.* **48** (10), e2021GL092919.
- BERTIN, V. 2023 Similarity solutions in elastohydrodynamic bouncing. *arXiv preprint arXiv:2308.10754*.
- BIANCE, A.-L., CHEVY, F., CLANET, C., LAGUBEAU, G. & QUÉRÉ, D. 2006 On the elasticity of an inertial liquid shock. *J. Fluid Mech.* **554**, 47–66.
- BILOTTO, J., KOLINSKI, J. M., LECAMPION, B., MOLINARI, J.-F., SUBHASH, G. & GARCIA-SUAREZ, J. 2023 Fluid-mediated impact of soft solids. *arXiv preprint arXiv:2311.09953*.
- BONN, D., EGGLERS, J., INDEKEU, J., MEUNIER, J. & ROLLEY, E. 2009 Wetting and spreading. *Rev. Mod. Phys.* **81** (2), 739–805.
- BORMASHENKO, E., POGREB, R., WHYMAN, G. & ERLICH, M. 2007 Resonance Cassie-Wenzel wetting transition for horizontally vibrated drops deposited on a rough surface. *Langmuir* **23** (24), 12217–12221.
- BOUROUIBA, L. 2021 The fluid dynamics of disease transmission. *Annu. Rev. Fluid Mech.* **53**, 473–508.
- BOUWHUIS, W., VAN DER VEEN, R. C. A., TRAN, T., KEIJ, D. L., WINKELS, K. G., PETERS, I. R., VAN DER MEER, D., SUN, C., SNOEIJER, J. H. & LOHSE, D. 2012 Maximal air bubble entrainment at liquid-drop impact. *Phys. Rev. Lett.* **109** (26), 264501.
- BRACKBILL, J. U., KOTHE, D. B. & ZEMACH, C. 1992 A continuum method for modeling surface tension. *J. Comput. Phys.* **100** (2), 335–354.
- CALLIES, M. & QUÉRÉ, D. 2005 On water repellency. *Soft Matter* **1** (1), 55–61.
- CHANTELLOT, P. 2018 Rebonds spéciaux de liquides. PhD thesis, Université Paris-Saclay (ComUE).
- CHEN, X., MA, R., LI, J., HAO, C., GUO, W., LUK, B. L., LI, S. C., YAO, S. & WANG, Z. 2012 Evaporation of droplets on superhydrophobic surfaces: surface roughness and small droplet size effects. *Phys. Rev. Lett.* **109** (11), 116101.
- CHENG, N.-S. 2008 Formula for the viscosity of a glycerol–water mixture. *Ind. Eng. Chem. Res.* **47** (9), 3285–3288.
- CHENG, X., SUN, T.-P. & GORDILLO, L. 2022 Drop impact dynamics: impact force and stress distributions. *Annu. Rev. Fluid Mech.* **54**, 57–81.
- CHEVY, F., CHEPELIANSKII, A., QUÉRÉ, D. & RAPHAËL, E. 2012 Liquid Hertz contact: softness of weakly deformed drops on non-wetting substrates. *Europhys. Lett.* **100** (5), 54002.
- CHO, H. J., PRESTON, D. J., ZHU, Y. & WANG, E. N. 2016 Nanoengineered materials for liquid–vapour phase-change heat transfer. *Nat. Rev. Mater.* **2** (2), 16092.
- CHUBYNSKY, M. V., BELOUSOV, K. I., LOCKERBY, D. A. & SPRITTLES, J. E. 2020 Bouncing off the walls: the influence of gas-kinetic and van der Waals effects in drop impact. *Phys. Rev. Lett.* **124**, 084501.
- CLANET, C., BÉGUIN, C., RICHARD, D. & QUÉRÉ, D. 2004 Maximal deformation of an impacting drop. *J. Fluid Mech.* **517**, 199–208.
- DA VINCI, L. 1508 *Codex Hammer* (earlier *Codex Leicester*). In *The Notebooks of Leonardo da Vinci* (ed. and trans. E. MacCurdy).. George Braziller.
- DE GENNES, P. G. 1985 Wetting: statics and dynamics. *Rev. Mod. Phys.* **57**, 827–863.
- DENG, X., MAMMEN, L., BUTT, H.-J. & VOLLMER, D. 2012 Candle soot as a template for a transparent robust superamphiphobic coating. *Science* **335** (6064), 67–70.
- DRISCOLL, M. M. & NAGEL, S. R. 2011 Ultrafast interference imaging of air in splashing dynamics. *Phys. Rev. Lett.* **107** (15), 154502.

- 517 EGGERS, J., FONTELOS, M. A., JOSSERAND, C. & ZALESKI, S. 2010 Drop dynamics after  
518 impact on a solid wall: theory and simulations. *Phys. Fluids* **22** (6), 062101.
- 519 FUKAI, J., SHIIBA, Y., YAMAMOTO, T., MIYATAKE, O., POULIKAKOS, D., MEGARIDIS, C. M.  
520 & ZHAO, Z. 1995 Wetting effects on the spreading of a liquid droplet colliding with a flat  
521 surface: experiment and modeling. *Phys. Fluids* **7**, 236–247.
- 522 GARCÍA-GEIJO, P., RIBOUX, G. & GORDILLO, JM 2024 The skating of drops impacting over gas  
523 or vapour layers. *J. Fluid Mech.* **980**, A35.
- 524 GAUTHIER, A., SYMON, S., CLANET, C. & QUÉRÉ, D. 2015 Water impacting on  
525 superhydrophobic macrotextures. *Nat. Commun.* **6** (1), 1–6.
- 526 GOHARDANI, O. 2011 Impact of erosion testing aspects on current and future flight conditions.  
527 *Prog. Aerosp. Sci.* **47** (4), 280–303.
- 528 GORDILLO, J. M., RIBOUX, G. & QUINTERO, E. S. 2019 A theory on the spreading of impacting  
529 droplets. *J. Fluid Mech.* **866**, 298–315.
- 530 GORDILLO, L., SUN, T.-P. & CHENG, X. 2018 Dynamics of drop impact on solid surfaces:  
531 evolution of impact force and self-similar spreading. *J. Fluid Mech.* **840**, 190–214.
- 532 GORIN, B., DI MAURO, G., BONN, D. & KELLAY, H. 2022 Universal aspects of droplet spreading  
533 dynamics in Newtonian and non-Newtonian fluids. *Langmuir* **38** (8), 2608–2613.
- 534 HAO, C., LIU, Y., CHEN, X., LI, J., ZHANG, M., ZHAO, Y. & WANG, Z. 2016 Bioinspired  
535 interfacial materials with enhanced drop mobility: from fundamentals to multifunctional  
536 applications. *Small* **12** (14), 1825–1839.
- 537 HE, L., DING, L., LI, B., MU, W., LI, P. & LIU, F. 2021 Optimization strategy to  
538 inhibit droplets rebound on pathogen-modified hydrophobic surfaces. *ACS Appl. Mater.  
539 Interfaces* **13** (32), 38018–38028.
- 540 HOFFMAN, H., SIJS, R., DE GOEDE, T. & BONN, D. 2021 Controlling droplet deposition with  
541 surfactants. *Phys. Rev. Fluids* **6** (3), 033601.
- 542 JHA, A., CHANTELOT, P., CLANET, C. & QUÉRÉ, D. 2020 Viscous bouncing. *Soft Matter* **16**,  
543 7270–7273.
- 544 JI, B., YANG, Z. & FENG, J. 2021 Compound jetting from bubble bursting at an air-oil-water  
545 interface. *Nat. Commun.* **12** (1), 6305.
- 546 JIN, P., ZHAO, K., BLIN, Z., ALLAIS, M., MOUTERDE, T. & QUÉRÉ, D. 2023 When marbles  
547 challenge pearls. *J. Chem. Phys.* **158** (20).
- 548 JOSSERAND, C. & THORODDSEN, S. T. 2016 Drop impact on a solid surface. *Annu. Rev. Fluid  
549 Mech.* **48**, 365–391.
- 550 JOWKAR, S. & MORAD, M. R. 2019 Rebounding suppression of droplet impact on hot surfaces:  
551 effect of surface temperature and concaveness. *Soft Matter* **15** (5), 1017–1026.
- 552 KIM, J. 2007 Spray cooling heat transfer: The state of the art. *Int. J. Heat Fluid Flow* **28** (4),  
553 753–767.
- 554 KIM, S., WU, Z., ESMAILI, E., DOMBROSKIE, J. J & JUNG, S. 2020 How a raindrop gets  
555 shattered on biological surfaces. *Proc. Natl. Acad. Sci. U.S.A.* **117** (25), 13901–13907.
- 556 KOLINSKI, J. M., MAHADEVAN, L. & RUBINSTEIN, S. M. 2014 Drops can bounce from perfectly  
557 hydrophilic surfaces. *Europhys. Lett.* **108**, 24001.
- 558 KOOIJ, S., SIJS, R., DENN, M. M., VILLERMAUX, E. & BONN, D. 2018 What determines the  
559 drop size in sprays? *Phys. Rev. X* **8** (3), 031019.
- 560 LAAN, N., DE BRUIN, K. G., BARTOLO, D., JOSSERAND, C. & BONN, D. 2014 Maximum  
561 diameter of impacting liquid droplets. *Phys. Rev. Appl.* **2** (4), 044018.
- 562 LAFUMA, A. & QUÉRÉ, D. 2003 Superhydrophobic states. *Nat. Mater.* **2** (7), 457–460.
- 563 LANGLEY, K., LI, E. Q. & THORODDSEN, S. T. 2017 Impact of ultra-viscous drops: air-film  
564 gliding and extreme wetting. *J. Fluid Mech.* **813**, 647–666.
- 565 LESSER, M. B. 1981 Analytic solution of liquid-drop impact problems. *Proc. R. Soc. Lond. A*  
566 **377** (1770), 289–308.
- 567 LI, J., ZHANG, B., GUO, P. & LV, Q. 2014 Impact force of a low speed water droplet colliding  
568 on a solid surface. *J. Appl. Phys.* **116** (21), 214903.
- 569 LI, Y., QUÉRÉ, D., LV, C. & ZHENG, Q. 2017 Monostable superrepellent materials. *Proc. Natl  
570 Acad. Sci. USA* **114** (13), 3387–3392.
- 571 LIU, M., WANG, S. & JIANG, L. 2017 Nature-inspired superwettability systems. *Nat. Rev.  
572 Mater.* **2** (7), 17036.

- LOHSE, D. 2022 Fundamental fluid dynamics challenges in inkjet printing. *Annu. Rev. Fluid Mech.* **54**, 349–382.
- LOHSE, D. & VILLERMAUX, E. 2020 Double threshold behavior for breakup of liquid sheets. *Proc. Natl. Acad. Sci. U.S.A.* **117**, 18912–18914.
- MA, Y. & HUANG, H. 2023 Scaling maximum spreading of droplet impacting on flexible substrates. *J. Fluid Mech.* **958**, A35.
- MANDRE, S., MANI, M. & BRENNER, M. P. 2009 Precursors to splashing of liquid droplets on a solid surface. *Phys. Rev. Lett.* **102** (13), 134502.
- MARTOZET, G., JØRGENSEN, L., PELET, Y., BIANCE, A.-L. & BARENTIN, C. 2021 Dynamic arrest during the spreading of a yield stress fluid drop. *Phys. Rev. Fluids* **6** (4), 044006.
- MIRELS, H. 1955 Laminar boundary layer behind shock advancing into stationary fluid. *NACA TN* **3401**, 25.
- MITCHELL, B. R., KLEWICKI, J. C., KORKOLIS, Y. P. & KINSEY, B. L. 2019 The transient force profile of low-speed droplet impact: measurements and model. *J. Fluid Mech.* **867**, 300–322.
- MOLÁČEK, J. & BUSH, J. W. M. 2012 A quasi-static model of drop impact. *Phys. Fluids* **24** (12), 127103.
- NEARING, M. A., BRADFORD, J. M. & HOLTZ, R. D. 1986 Measurement of force vs. time relations for waterdrop impact. *Soil Sci. Soc. Am. J.* **50**, 1532–1536.
- PAPADOPOULOS, P., MAMMEN, L., DENG, X., VOLLMER, D. & BUTT, H.-J. 2013 How superhydrophobicity breaks down. *Proc. Natl. Acad. Sci. USA* **110** (9), 3254–3258.
- PHILIPPI, J., LAGRÉE, P.-Y. & ANTKOWIAK, A. 2016 Drop impact on a solid surface: short-time self-similarity. *J. Fluid Mech.* **795**, 96–135.
- PÖHLKER, M. L., PÖHLKER, C., KRÜGER, O. O., FÖRSTER, J.-D., BERKEMEIER, T., ELBERT, W., FRÖHLICH-NOWOISKY, J., PÖSCHL, U., BAGHERI, G., BODENSCHATZ, E., HUFFMAN, J. A., SCHEITHAUER, S. & MIKHAILOV, E. 2023 Respiratory aerosols and droplets in the transmission of infectious diseases. *Rev. Mod. Phys.* **95** (4), 045001.
- POPINET, S. 2009 An accurate adaptive solver for surface-tension-driven interfacial flows. *J. Comput. Phys.* **228** (16), 5838–5866.
- POPINET, S. 2018 Numerical models of surface tension. *Annu. Rev. Fluid Mech.* **50**, 49–75.
- POPINET, S. & COLLABORATORS 2013–2023 Basilisk C: volume of fluid method. <http://basilisk.fr> (Last accessed: August 23, 2023).
- QUÉRÉ, D. 2008 Wetting and roughness. *Annu. Rev. Mater. Res.* **38**, 71–99.
- RAMÍREZ-SOTO, O., SANJAY, V., LOHSE, D., PHAM, J. T. & VOLLMER, D. 2020 Lifting a sessile drop from a superamphiphobic surface with an impacting one. *Sci. Adv.* **6**, eaba4330.
- REIN, M. 1993 Phenomena of liquid drop impact on solid and liquid surfaces. *Fluid Dyn. Res.* **12**, 61–93.
- RENARDY, Y., POPINET, S., DUCHEMIN, L., RENARDY, M., ZALESKI, S., JOSSERAND, C., DRUMRIGHT-CLARKE, M. A., RICHARD, D., CLANET, C. & QUÉRÉ, D. 2003 Pyramidal and toroidal water drops after impact on a solid surface. *J. Fluid Mech.* **484**, 69–83.
- RIBOUX, G. & GORDILLO, J. M. 2014 Experiments of drops impacting a smooth solid surface: a model of the critical impact speed for drop splashing. *Phys. Rev. Lett.* **113** (2), 024507.
- RICHARD, D., CLANET, C. & QUÉRÉ, D. 2002 Contact time of a bouncing drop. *Nature* **417** (6891), 811–811.
- RICHARD, D. & QUÉRÉ, D. 2000 Bouncing water drops. *Europhys. Lett.* **50** (6), 769–775.
- SANJAY, V. 2022 Viscous Free-Surface Flows. PhD thesis, University of Twente.
- SANJAY, V. 2023 VatsalSy/Impact-forces-of-water-drops-falling-on- superhydrophobic-surfaces: Impact Forces of Water Drops Falling on Superhydrophobic Surfaces. <https://doi.org/10.5281/zenodo.7598181>.
- SANJAY, V., CHANTELOT, P. & LOHSE, D. 2023a When does an impacting drop stop bouncing? *Journal of Fluid Mechanics* **958**, A26.
- SANJAY, V., LAKSHMAN, S., CHANTELOT, P., SNOEIJER, J. H. & LOHSE, D. 2023b Drop impact on viscous liquid films. *J. Fluid Mech.* **958**, A25.
- SANJAY, V. & LOHSE, D. 2024 The unifying theory of scaling in drop impact: forces & maximum spreading diameter. *In preparation*.
- SANJAY, V., LOHSE, D. & JALAAL, M. 2021 Bursting bubble in a viscoplastic medium. *J. Fluid Mech.* **922**, A2.

- SANJAY, V., SEN, U., KANT, P. & LOHSE, D. 2022 Taylor-Culick retractions and the influence of the surroundings. *J. Fluid Mech.* **948**, A14.
- SBRAGAGLIA, M., PETERS, A. M., PIRAT, C., BORKENT, B. M., LAMMERTINK, R. G. H., WESSLING, M. & LOHSE, D. 2007 Spontaneous breakdown of superhydrophobicity. *Phys. Rev. Lett.* **99** (15), 156001.
- SCHLICHTING, H. 1968 *Boundary-layer theory*. McGraw-Hill.
- SCHROLL, R. D., JOSSERAND, C., ZALESKI, S. & ZHANG, W. W. 2010 Impact of a viscous liquid drop. *Phys. Rev. Lett.* **104** (3), 034504.
- SHARMA, P. K. & DIXIT, H. N. 2021 Regimes of wettability-dependent and wettability-independent bouncing of a drop on a solid surface. *J. Fluid Mech.* **908**, A37.
- SHIRI, S. & BIRD, J. C. 2017 Heat exchange between a bouncing drop and a superhydrophobic substrate. *Proc. Natl. Acad. Sci. U.S.A.* **114** (27), 6930–6935.
- SIJS, R. & BONN, D. 2020 The effect of adjuvants on spray droplet size from hydraulic nozzles. *Pest. Manage. Sci.* **76** (10), 3487–3494.
- SMITH, F. R. & BRUTIN, D. 2018 Wetting and spreading of human blood: recent advances and applications. *Curr. Opin. Colloid Interface Sci.* **36**, 78–83.
- SMITH, F. R., NICLOUX, C. & BRUTIN, D. 2018 Influence of the impact energy on the pattern of blood drip stains. *Phys. Rev. Fluids* **3** (1), 013601.
- SMITH, M. I. & BERTOLA, V. 2010 Effect of polymer additives on the wetting of impacting droplets. *Phys. Rev. Lett.* **104**, 154502.
- SOTO, D., DE LARIVIERE, A. B., BOUTILLON, X., CLANET, C. & QUÉRÉ, D. 2014 The force of impacting rain. *Soft Matter* **10** (27), 4929–4934.
- SPRITLES, JAMES E 2024 Gas microfilms in droplet dynamics: When do drops bounce? *Annu. Rev. Fluid Mech.* **56**, 91–118.
- THORAVAL, M.-J., SCHUBERT, J., KARPITSCHKA, S., CHANANA, M., BOYER, F., SANDOVAL-NAVAL, E., DIJKSMAN, J. F., SNOEIJER, J. H. & LOHSE, D. 2021 Nanoscopic interactions of colloidal particles can suppress millimetre drop splashing. *Soft Matter* **17** (20), 5116–5121.
- THORAVAL, M.-J., TAKEHARA, K., ETOH, T. G. & THORODDSEN, S. T. 2013 Drop impact entrapment of bubble rings. *J. Fluid Mech.* **724**, 234–258.
- TSAI, P., LAMMERTINK, R. G. H., WESSLING, M. & LOHSE, D. 2010 Evaporation-triggered wetting transition for water droplets upon hydrophobic microstructures. *Phys. Rev. Lett.* **104** (11), 116102.
- TUTEJA, A., CHOI, W., MA, M., MABRY, J. M., MAZZELLA, S. A., RUTLEDGE, G. C., MCKINLEY, G. H. & COHEN, R. E. 2007 Designing superoleophobic surfaces. *Science* **318** (5856), 1618–1622.
- VILLERMAUX, E. 2020 Fragmentation versus cohesion. *J. Fluid Mech.* **898**, P1.
- VILLERMAUX, E. & BOSSA, B. 2011 Drop fragmentation on impact. *J. Fluid Mech.* **668**, 412–435.
- VILLERMAUX, E., WANG, X. & DEIKE, L. 2022 Bubbles spray aerosols: certitudes and mysteries. *Proc. Natl. Acad. Sci. Nexus* **1** (5), pgac261.
- VOLK, A. & KÄHLER, C. J. 2018 Density model for aqueous glycerol solutions. *Exp. Fluids* **59** (5), 75.
- WAGNER, H. 1932 Über Stoß- und Gleitvorgänge an der Oberfläche von Flüssigkeiten. *Z. Angew. Math. Mech.* **12** (4), 193–215.
- WILDEMAN, S., VISSER, C. W., SUN, C. & LOHSE, D. 2016 On the spreading of impacting drops. *J. Fluid Mech.* **805**, 636–655.
- WORTHINGTON, A. M. 1876a On the forms assumed by drops of liquids falling vertically on a horizontal plate. *Proc. R. Soc.* **25** (171–178), 261–272.
- WORTHINGTON, A. M. 1876b A second paper on the forms assumed by drops of liquids falling vertically on a horizontal plate. *Proc. R. Soc.* **25** (171–178), 498–503.
- WU, S., DU, Y., ALSAID, Y., WU, D., HUA, M., YAN, Y., YAO, B., MA, Y., ZHU, X. & HE, X. 2020 Superhydrophobic photothermal icephobic surfaces based on candle soot. *Proc. Natl. Acad. Sci. USA* **117** (21), 11240–11246.
- XU, L., ZHANG, W. W. & NAGEL, S. R. 2005 Drop splashing on a dry smooth surface. *Phys. Rev. Lett.* **94** (18), 184505.

- 686 YARIN, A. L. 2006 Drop impact dynamics: splashing, spreading, receding, bouncing... *Annu.*  
687 *Rev. Fluid Mech.* **38**, 159–192.
- 688 YARIN, A. L., ROISMAN, I. V. & TROPEA, C. 2017 *Collision Phenomena in Liquids and Solids*.  
689 Cambridge University Press.
- 690 YUN, S. 2017 Bouncing of an ellipsoidal drop on a superhydrophobic surface. *Sci. Rep.* **7** (1),  
691 17699.
- 692 ZHANG, B., LI, J., GUO, P. & LV, Q. 2017 Experimental studies on the effect of reynolds and  
693 weber numbers on the impact forces of low-speed droplets colliding with a solid surface.  
694 *Exp. Fluids* **58** (9), 1–12.
- 695 ZHANG, B., SANJAY, V., SHI, S., ZHAO, Y., LV, C. & LOHSE, D. 2022 Impact forces of water  
696 drops falling on superhydrophobic surfaces. *Phys. Rev. Lett.* **129**, 104501.
- 697 ZHANG, R., ZHANG, B., LV, Q., LI, J. & GUO, P. 2019 Effects of droplet shape on impact  
698 force of low-speed droplets colliding with solid surface. *Exp. Fluids* **60** (4), 64.
- 699 ZHENG, S., DILLAVOU, S. & KOLINSKI, J. M. 2021 Air mediates the impact of a compliant  
700 hemisphere on a rigid smooth surface. *Soft Matter* **17** (14), 3813–3819.